

Blue straggler stars beyond the Milky Way. II. A binary origin for blue straggler stars in Magellanic Cloud clusters

WEIJIA SUN,¹ CHENGYUAN LI,^{2,3} RICHARD DE GRIJS,^{2,4} AND LICAI DENG^{5,6,3}

¹*Kavli Institute for Astronomy & Astrophysics and Department of Astronomy, Peking University, Yi He Yuan Lu 5, Hai Dian District, Beijing 100871, China*

²*Department of Physics and Astronomy, Macquarie University, Balaclava Road, Sydney, NSW 2109, Australia*

³*Department of Astronomy, China West Normal University, Nanchong 637002, China*

⁴*International Space Science Institute–Beijing, 1 Nanertiao, Zhongguancun, Beijing 100190, China*

⁵*Key Laboratory for Optical Astronomy, National Astronomical Observatories, Chinese Academy of Sciences, 20A Datun Road, Chaoyang District, Beijing 100012, China*

⁶*School of Astronomy and Space Science, University of the Chinese Academy of Sciences, Huairou 101408, China*

ABSTRACT

We have analyzed populations of blue straggler stars (BSSs) in 24 Magellanic Cloud star clusters using multi-passband *Hubble Space Telescope* images. We compiled a homogeneous BSS database, containing both traditional and evolved BSSs. We uncovered a sub-linear correlation between the number of BSSs in the cluster cores and the clusters’ core masses, characterized by a power-law index of 0.51 ± 0.07 . For low stellar collision rates, the mass-normalized number of BSSs depends only weakly (or perhaps not at all) on the collision rate, implying that the binary-driven BSS formation channel dominates. Comparison with simulations suggests that stellar collisions contribute less than 20% to the total number of BSSs formed. Further tests, including analysis of the BSS specific frequencies and their population numbers at larger cluster radii, suggest that binary interactions may be their main formation channel, hinting at an anti-correlation between a cluster’s binary fraction and its core mass.

Keywords: blue stragglers — star clusters: general — Magellanic Clouds

1. INTRODUCTION

Blue straggler stars (BSSs) are brighter and bluer than the main-sequence turnoff (MSTO) in a given star cluster, yet they occupy the extrapolation of a cluster’s main sequence as defined by its bulk stellar population. Since they were first discovered in the globular cluster (GC) M3 by Sandage (1953), BSSs have been found in all known GCs (Piotto et al. 2004), as well as in open clusters (Chen & Han 2008) and dwarf galaxies (Mapelli et al. 2007).

The prevailing scenarios for the formation of BSSs involve direct collisions of single stars and/or binary systems (McCrea 1964; Ferraro et al. 2003) or mass transfer and/or the coalescence of primordial binaries (Iben & Tutukov 1984; Knigge et al. 2009; Leigh et al. 2013). We must examine the entire population of BSSs in clusters in order to distinguish between the different formation mechanisms. The first attempt to do so was made by Ferraro et al. (2003), who compared the predicted number of collisional BSSs with actual observations in six GCs and found good agreement between both numbers for most clusters, except for the lowest-density GC. However, Piotto et al. (2004) detected a weak anti-correlation of the numbers of BSSs with the theoretical collision rate (see below), thus indicating that collisions cannot be the main source of the observed populations of BSSs.

Knigge et al. (2009) found a robust correlation with an intrinsic cluster property for their sample of 57 Galactic GCs: the number of BSSs in a cluster’s core exhibits a ‘sub-linear’ correlation with the cluster’s core mass, $N_{\text{BSS,core}} \propto M_c^{0.5}$. This can be understood as the result of binary interactions if the binary fraction also depends on the core mass, i.e., $f_{\text{bin}} \propto M_c^{-0.5}$ (Milone et al. 2012). However, Leigh et al. (2013) found that including the numbers of binary stars in the cores of 30 additional Galactic GCs did not strengthen the correlation; the resulting degradation of the correlation further complicated the underlying issue as regards the origin of BSSs.

Indeed, the distinction between both formation channels is not as clear-cut in real environments. On the one hand, a cluster’s core binary fraction is strongly regulated by dynamical interactions (Fregeau et al. 2009), thus directly influencing the formation rate of BSSs. On the other, under some conditions, collisions are more probable to occur between binary stars because of their large cross sections (Leigh et al. 2011b). Increasing lines of evidence suggest

that both formation channels are closely linked. [Mapelli et al. \(2006\)](#) argued that the different origins of BSSs may be related to their spatial distribution: BSSs in a cluster’s periphery then form through mass transfer, whereas BSSs close to the cluster core most likely have a collisional origin. Another piece of evidence came from the two distinct sequences of BSSs observed in the color–magnitude diagram (CMD) of M30 ([Ferraro et al. 2009](#)).

To provide a better understanding of the prevailing BSS formation mechanisms, we need to expand our samples to include younger and more distant objects. Thus far, only a few studies have focused on extragalactic GCs ([Li et al. 2013](#); [Li & Hong 2018](#)). The Magellanic Clouds (MCs) host numerous clusters spanning a broad range of ages ([McLaughlin & van der Marel 2005](#)). C. Li et al. (submitted) discovered a branch of evolved stars which are much brighter than the normal evolved stars in their host clusters. The most straightforward interpretation of these stars is that they are all younger than the cluster’s bulk stellar population. Based on isochrone fitting, they found that the masses of these young evolved stars are generally lower than twice the average mass of their normal counterparts. Thus, Li et al. attributed the origin of this younger population to evolved BSSs—BSSs having evolved off the MS—which had already been identified in the Galactic GCs M3, M13 ([Ferraro et al. 1997](#)), and M80 ([Ferraro et al. 1999](#)). [Parada et al. \(2016\)](#) reported a total number of evolved BSSs in the Galactic GC 47 Tucanae (47 Tuc) that was comparable to the number of BSSs observed, leading them to suggest a much shorter BSS lifetime than previously thought.

In this paper, we analyze 24 clusters in the MCs. We uncover a sub-linear correlation between the number of BSSs in the cluster cores and the clusters’ core masses, with a power-law index of 0.49 ± 0.09 . The mass-normalized number of BSSs is only weakly dependent on the mass-normalized collision parameter and, for higher collision rates, it decreases with increasing collision parameter, clearly indicating the predominance of binary disruption. Therefore we conclude that the formation of the observed BSSs is likely dominated by binary mechanisms, at least in most of our sample clusters.

This article is organized as follows. In Section 2 we present the observations and data reduction procedures applied. Section 3 reports our main results, including any correlations and anti-correlations with cluster properties. Next, we discuss the possible BSS formation channels in Section 4. Finally, we summarize our study in Section 5.

2. OBSERVATIONS AND DATA REDUCTION

2.1. Photometry

The clusters in the present paper were selected from the *Hubble Space Telescope* (*HST*) Data Archive at the Space Telescope Science Institute. We collected observational data obtained with the Advanced Camera for Surveys/Wide Field Channel (ACS/WFC) and the Wide Field Camera 3/Ultraviolet and Visible channel (WFC3/UVIS). Most cluster data sets included a nearby ‘reference’ field, which we used to statistically estimate the contribution from the background/field stellar population. For clusters without a reference field, we only selected those objects with sizes that were sufficiently small that an edge of the science image could be used for field correction purposes and to derive reliable structural parameters. [Raso et al. \(2017\)](#) argued that UV-based surveys are more efficient in identifying BSSs than optical surveys. However, although for some clusters ultraviolet (UV) observations were available (e.g., *HST* program GO-14164; PI: A. Sarajedini), we nevertheless only based our selection on the presence of data in optical passbands. This was done because only very few clusters were observed at UV wavelengths and we prefer to establish a homogeneous observational basis for our work. We selected all intermediate-age (1–3 Gyr-old) and old (~ 10 Gyr-old) clusters in the MCs for which suitable *HST* observations were available (for more details, see Section 2.3). Young massive clusters were excluded, because these clusters do not exhibit a clear MSTO point, which renders the selection of BSSs unclear. Detailed information about our 24 sample clusters is presented in Table 1.

Table 1. Summary of the *HST* observations of our Magellanic Cloud cluster (MCC) sample.

Cluster	Galaxy	Camera	Exposure Time	Filter	ID	PI
ESO057–SC075	LMC	ACS/WFC	25 s + 340 s × 2	F555W	10595	P. Goudfrooij
			15 s + 340 s × 2	F814W		
Hodge 11	LMC	ACS/WFC	50 s × 2 + 345 s × 6 + 370 s × 6	F606W	14164	A. Sarajedini
			70 s × 2 + (345 s + 377 s + 410 s) × 6	F814W		
Hodge 11 (Ref)		ACS/WFC	550 s × 4 + 570 s × 8	F435W	14164	A. Sarajedini

Table 1 continued on next page

Table 1 (continued)

Cluster	Galaxy	Camera	Exposure Time	Filter	ID	PI
			$50\text{ s} + 570\text{ s} \times 3$	F606W		
IC 2146	LMC	ACS/WFC	250 s	F555W	9891	G. Gilmore
			170 s	F814W		
NGC 1466	LMC	ACS/WFC	$50\text{ s} \times 2 + 353\text{ s} \times 12$	F606W	14164	A. Sarajedini
			$70\text{ s} \times 2 + (352\text{ s} + 385\text{ s} + 420\text{ s}) \times 6$	F814W		
NGC 1466 (Ref)		ACS/WFC	$575\text{ s} \times 12$	F435W	14164	A. Sarajedini
			$50\text{ s} + 566\text{ s} \times 3$	F606W		
NGC 1644	LMC	ACS/WFC	250 s	F555W	9891	G. Gilmore
			170 s	F814W		
NGC 1651	LMC	WFC3/UVIS	$120\text{ s} + 600\text{ s} + 720\text{ s}$	F475W	12257	L. Girardi
			$30\text{ s} + 700\text{ s} \times 2$	F814W		
NGC 1651 (Ref)		ACS/WFC	$500\text{ s} \times 2$	F475W	12257	L. Girardi
			$500\text{ s} \times 2$	F814W		
NGC 1652	LMC	ACS/WFC	300 s	F555W	9891	G. Gilmore
			200 s	F814W		
NGC 1718	LMC	WFC3/UVIS	$120\text{ s} + 600\text{ s} + 720\text{ s}$	F475W	12257	L. Girardi
			$30\text{ s} + 700\text{ s} \times 2$	F814W		
NGC 1718 (Ref)		ACS/WFC	$500\text{ s} \times 2$	F475W	12257	L. Girardi
			$500\text{ s} \times 2$	F814W		
NGC 1783	LMC	ACS/WFC	$40\text{ s} + 340\text{ s} \times 2$	F555W	10595	P. Goudfrooij
			$8\text{ s} + 340\text{ s} \times 2$	F814W		
NGC 1783 (Ref)		ACS/WFC	$80\text{ s} + 300\text{ s} \times 2$	F814W	12257	L. Girardi
			$350\text{ s} \times 2$	F555W		
NGC 1806	LMC	ACS/WFC	$40\text{ s} + 340\text{ s} \times 2$	F555W	10595	P. Goudfrooij
			$8\text{ s} + 340\text{ s} \times 2$	F814W		
NGC 1806 (Ref)		ACS/WFC	$80\text{ s} + 300\text{ s} + 340\text{ s}$	F814W	12257	L. Girardi
			$350\text{ s} \times 2$	F555W		
NGC 1831	LMC	WFC3/UVIS	$100\text{ s} + 660\text{ s} + 720\text{ s}$	F814W	14688	P. Goudfrooij
			$975\text{ s} \times 2 + 1115\text{ s} \times 2$	F336W		
NGC 1831 (Ref)		ACS/WFC	$850\text{ s} + 890\text{ s} + 980\text{ s}$	F435W	14688	P. Goudfrooij
			$600\text{ s} + 950\text{ s}$	F814W		
NGC 1841	LMC	ACS/WFC	$50\text{ s} \times 2 + 353\text{ s} \times 12$	F606W	14164	A. Sarajedini
			$70\text{ s} \times 2 + (352\text{ s} + 385\text{ s} + 420\text{ s}) \times 6$	F814W		
NGC 1841 (Ref)		ACS/WFC	$575\text{ s} \times 12$	F435W	14164	A. Sarajedini
			$50\text{ s} + 566\text{ s} \times 3$	F606W		
NGC 1846	LMC	ACS/WFC	$40\text{ s} + 340\text{ s} \times 2$	F555W	10595	P. Goudfrooij
			$8\text{ s} + 340\text{ s} \times 2$	F814W		
NGC 1846 (Ref)	LMC	WFC3/UVIS	$348\text{ s} \times 2$	F555W	12326	K. Noll
			$400\text{ s} \times 2$	F814W		
NGC 1852	LMC	ACS/WFC	330 s	F555W	9891	G. Gilmore
			200 s	F814W		
NGC 1852 (Ref)		ACS/WFC	$500\text{ s} \times 2$	F555W	12257	L. Girardi
			$350\text{ s} \times 2$	F814W		
NGC 1868	LMC	WFC3/UVIS	$90\text{ s} + 666\text{ s}$	F814W	14710	A. Milone
			$830\text{ s} + 831\text{ s} \times 2$	F336W		
NGC 1868 (Ref)		ACS/WFC	$42\text{ s} + 530\text{ s} + 827\text{ s}$	F814W	14710	A. Milone
			$667\text{ s} + 679\text{ s} + 703\text{ s} + 760\text{ s}$	F475W		
NGC 1978	LMC	ACS/WFC	300 s	F555W	9891	G. Gilmore
			200 s	F814W		
NGC 1978 (Ref)		ACS/WFC	$500\text{ s} \times 2$	F555W	12257	L. Girardi
			$350\text{ s} \times 2$	F814W		
NGC 2154	LMC	ACS/WFC	300 s	F555W	9891	G. Gilmore
			200 s	F814W		
NGC 2154 (Ref)		ACS/WFC	$500\text{ s} \times 2$	F555W	12257	L. Girardi

Table 1 continued on next page

Table 1 (continued)

Cluster	Galaxy	Camera	Exposure Time	Filter	ID	PI
			350 s × 2	F814W		
NGC 2173	LMC	WFC3/UVIS	30 s + 550 s + 700 s × 2	F814W	12257	L. Girardi
			120 s + 700 s × 2	F475W		
NGC 2173 (Ref)		ACS/WFC	90 s + 500 s × 2 + 700 s × 2	F475W	12257	L. Girardi
			10 s + 600 s + 690 s + 700 s × 2	F814W		
NGC 2203	LMC	WFC3/UVIS	30 s + 550 s + 700 s × 2	F814W	12257	L. Girardi
			120 s + 700 s × 2	F475W		
NGC 2203 (Ref)		ACS/WFC	90 s + 500 s × 2 + 700 s × 2	F475W	12257	L. Girardi
			10 s + 550 s + 690 s + 713 s × 2	F814W		
NGC 2209	LMC	WFC3/UVIS	60 s + 485 s × 2	F814W	12908	P. Goudfrooij
			850 s × 2	F438W		
NGC 2209 (Ref)		ACS/WFC	361 s + 383 s	F814W	12908	P. Goudfrooij
			820 s + 840 s	F435W		
NGC 2213	LMC	WFC3/UVIS	120 s + 600 s + 720 s	F475W	12257	L. Girardi
			30 s + 700 s × 2	F814W		
NGC 2213 (Ref)		ACS/WFC	500 s × 2	F475W	12257	L. Girardi
			500 s × 2	F814W		
NGC 2249	LMC	WFC3/UVIS	60 s + 425 s × 2	F814W	12908	P. Goudfrooij
			825 s × 2	F438W		
NGC 2249 (Ref)		ACS/WFC	333 s + 413 s	F814W	12908	P. Goudfrooij
			795 s + 815 s	F435W		
NGC 2257	LMC	ACS/WFC	50 s × 2 + 353 s × 6 + 364 s × 3 + 525 s × 2	F606W	14164	A. Sarajedini
			70 s × 2 + (363 s + 400 s) × 6 + 390 s × 3 + 450 s × 2	F814W		
NGC 2257 (Ref)		ACS/WFC	575 s × 12	F435W	14164	A. Sarajedini
			50 s + 570 s × 3	F606W		
NGC 419	SMC	ACS/WFC	10 s × 2 + 474 s × 4	F814W	10396	J. Gallagher
			20 s × 2 + 496 s × 4	F555W		
NGC 419 (Ref)		ACS/WFC	60 s + 350 s + 400 s	F555W	12257	L. Girardi
			350 s + 400 s × 2	F814W		

We used the DOLPHOT2.0 package (Dolphin 2000) to perform our point-spread-function photometry. DOLPHOT2.0 provides two useful parameters for our analysis, **sharpness** and **crowding**, which we can employ to reject misclassifications and other contaminants from the samples. A large **sharpness** value may imply the detection of a cosmic ray (positive value) or a blend, cluster, or galaxy (negative value). The **crowding** parameter tells us how much brighter the star would have been measured had nearby stars not been fitted simultaneously. High **crowding** values are generally a sign of poorly measured stars. We rejected all objects with signal-to-noise ratios of less than 5 with absolute DOLPHOT2.0 **sharpness** parameter ≥ 0.2 or DOLPHOT2.0 **crowding** parameter ≥ 0.5 . These selection choices only affect of order 3% of the total numbers of stars brighter than 2 mag below the MSTO.

2.2. Artificial Star Tests

In order to characterize the photometric uncertainties and the completeness levels of the *HST* data, $\sim 60,000$ artificial stars were placed in both the cluster and reference fields using DOLPHOT2.0. The colors of the artificial stars were uniformly distributed on the CMD of the cluster, while the numbers were weighted so that larger numbers of fainter stars were generated. The stellar locations were randomly distributed across the field. For each run, we added 100 artificial stars so as not to significantly increase the degree of crowding in the images. The images were then reduced using the same measurement and selection procedures as applied to the real data. For the BSS populations, the completeness levels were close to 100% in both the cluster and reference fields. The completeness levels for stars brighter than 2 mag below the MSTO were typically higher than 90%. Completeness corrections were applied as and when necessary.

2.3. Cluster parameters

The cluster centers were determined based on the maximum spatial density in the cluster field, using a two-dimensional Gaussian kernel density estimator. We separated the cluster and reference fields into several radial annuli

and calculated their surface densities. The number of stars in each annulus was corrected for incompleteness and the (possibly fractional) annular area was calculated using a Monte Carlo-based method. In essence, large numbers of randomly distributed points were added and the number of points in a given annulus divided by the total number of points yielded the fraction of the area with respect to the total field of view.

While approximation of cluster profiles with a King profile (King 1962) is common practice for Galactic GCs, some evidence suggests that young clusters in weak tidal fields—such as those in the Large Magellanic Cloud—may not (yet) be tidally truncated. Instead, (Elson et al. 1989, EFF) profiles might be a better representation (Mackey & Gilmore 2003a,b). Thus we fitted the clusters’ surface densities using EFF profiles,

$$\rho(r) = \rho_0 \left(1 + \frac{r^2}{a^2} \right)^{-\gamma/2} + \rho_{\text{bkg}}, \quad (1)$$

where ρ_0 and ρ_{bkg} are the central and background surface densities, respectively. The core radius, a , and the power-law index, c , are linked to the King core radius, r_c , through

$$r_c = a(2^{2/\gamma} - 1)^{1/2}. \quad (2)$$

As regards those clusters for which we have a reference field available, both the cluster and reference fields were used for the surface density calculation. This approach provided excellent constraints on the level of field-star contamination. For clusters without a reference field, we only determined the structural parameters for those objects exhibiting clear radial decreases towards the science images’ outer regions. The typical uncertainty in the central coordinates of our intermediate-age clusters is smaller than 5 arcsec. Given their large sizes, however, the old clusters have relatively larger uncertainties associated with their structural parameters. The central coordinates of the old cluster NGC 1841 have the largest uncertainties of around 15 arcsec. Nevertheless, the center positions we derived deviates from that of Bica et al. (2008) by less than 5 arcsec. The same is true for the other clusters in our sample. For most of the intermediate-age clusters analyzed by Goudfrooij et al. (2014), we found a systematic difference in the resulting core radii, r_c , of less than 1 arcsec towards smaller values. This is likely driven by our approach to determining the structural parameters. Goudfrooij et al. (2014) only considered stars with higher completeness levels ($\geq 75\%$), which would result in a larger core if the completeness level within the core were relatively low. We confirmed that this systematic difference disappears if we adopt the same method. The only exception is NGC 1783, for which Goudfrooij et al. (2014) reported $r_c = 10.50 \pm 0.49$ pc. We note that literature derivations of this cluster’s core radius based on fitting King profiles are discrepant. Both Elson (1991) and Mucciarelli et al. (2007) found a core radius of around 5 pc for NGC 1783. Compared with Mackey & Gilmore (2003a); Piatti & Mackey (2018), we did not notice any significant differences in the core radii of our old sample clusters. The clusters’ structural parameters are included in Table 2.

We used the Padova group’s PARSEC 1.2S isochrones (Bressan et al. 2012) to perform our CMD fits based on visual inspection. In Table 3, we list the derived parameters: ages, metallicities, extinction values, and distance moduli. For most of our intermediate-age clusters, we found consistent best-fitting metallicity values of around $Z \sim 0.007$, with the exception of NGC 419. The same cluster data were analyzed by Niederhofer et al. (2016) using identical isochrone models. These latter authors adopted a fixed metallicity of $Z = 0.008$, which is consistent with our results to within 1σ . The only exception, NGC 419, is a star cluster in the Small Magellanic Cloud. It has a lower metallicity compared with its similarly aged counterparts in the Large Magellanic Cloud. Martocchia et al. (2017) found best-fitting parameters for NGC 419 of $\log(t \text{ yr}^{-1}) = 9.5$ and $Z = 0.0028$, indeed consistent with our results. As for the old clusters, we compared our results with Wagner-Kaiser et al. (2017) who used the same data but applied different methods to derive the distances. The deviations for all parameters between both sets of results are less than 2σ . We also derived the clusters’ central volume densities and their masses using the Monte Carlo method (for details, see the next section). Our estimates of these parameters are comparable to those of Mackey & Gilmore (2003a) and McLaughlin & van der Marel (2005) to within 1 to 2σ .

2.4. Characterization of the Stellar Populations

We selected the BSS populations in our intermediate-age sample clusters as follows: (a) they must be brighter than 2 mag below the MSTO; (b) they must also be brighter than the 250 Myr-old isochrone plus 3σ , where σ is the photometric uncertainty; (c) they must be bluer than the best-fitting isochrone for the cluster’s bulk stellar population minus 3σ . For our old clusters ($t \sim 10$ Gyr), we selected those stars that were bluer and brighter than the MSTO locus, located outside the 3σ envelope of the MSTO and the MS ridge line.

The evolved BSSs were identified using the same criteria as adopted by Li et al. In essence, they used an isochrone with an older age to fit the bulk stellar population, as well as two younger isochrones (see the blue dashed lines in Fig. 1) to roughly describe the bottom and top boundaries of the sample of bright, evolved stars. Next, as their evolved BSSs, they selected stars redder than the midpoint of the subgiant branch (SGB) and located either between these boundaries or within the 3σ envelopes of these young isochrones. Our selections of BSSs, evolved BSSs, and red giant-branch (RGB) stars, as well as the best-fitting isochrones are all indicated in Fig. 1.

Fig. Set 1. MC cluster CMDs

In this paper, we are most interested in the total number of BSSs in our clusters, rather than in their detailed distributions across the CMDs. Therefore, we did not apply a field-decontamination procedure using either stars located at the closest geometric distance in color-magnitude space (Niederhofer et al. 2015) or the number of stars in a cell of a given color-magnitude grid (Li et al. 2016). We simply calculated the total number of objects of a given stellar population in the cluster fields and subtracted the number of possible contaminating stars found in the field region, after correction for the size differences of these areas. All populations in our sample clusters returned positive values after field decontamination, implying that the stars we selected are most likely genuine cluster members.

3. ANALYSIS AND RESULTS

One method we can use to determine the contributions from various BSS formation channels is to derive the theoretical scaling laws and compare these with our observational data. The number of BSSs and its correlation with other cluster properties can potentially uncover the dominant formation mechanism. Although it is hard to tell how an individual BSS was formed based on a single photometric snapshot, we can still ascertain the predominant formation channel on a statistical basis.

We focused on the BSSs located in the cluster cores ($r \leq r_c$), where collisions are expected to be most frequent. If single-single stellar collisions are the main trigger of BSS formation, the number of BSSs in the cluster core should

Table 2. Structural parameters of our MC sample clusters.

Cluster	α_{J2000} (deg) ^a	δ_{J2000} (deg) ^a	a (pc)	γ	r_c (pc)
(1)	(2)	(3)	(4)	(5)	(6)
ESO057–SC075	$06^{\text{h}}13^{\text{m}}27.30^{\text{s}} \pm 0.39^{\text{s}}$	$-70^{\circ}41'43.57'' \pm 5.81''$	3.05 ± 0.41	2.07 ± 0.18	2.97 ± 0.15
Hodge 11	$06^{\text{h}}14^{\text{m}}22.92^{\text{s}} \pm 0.54^{\text{s}}$	$-69^{\circ}50'54.90'' \pm 8.03''$	4.37 ± 0.41	2.85 ± 0.17	3.46 ± 0.24
IC 2146	$05^{\text{h}}37^{\text{m}}47.43^{\text{s}} \pm 0.47^{\text{s}}$	$-74^{\circ}46'58.52'' \pm 7.06''$	8.75 ± 1.16	2.89 ± 0.43	6.86 ± 0.37
NGC 1466	$03^{\text{h}}44^{\text{m}}32.91^{\text{s}} \pm 0.25^{\text{s}}$	$-71^{\circ}40'09.85'' \pm 3.70''$	5.33 ± 0.78	4.12 ± 0.65	3.37 ± 0.21
NGC 1644	$04^{\text{h}}37^{\text{m}}40.13^{\text{s}} \pm 0.24^{\text{s}}$	$-66^{\circ}11'54.67'' \pm 3.57''$	2.68 ± 0.22	3.09 ± 0.17	2.02 ± 0.06
NGC 1651	$04^{\text{h}}37^{\text{m}}32.07^{\text{s}} \pm 0.33^{\text{s}}$	$-70^{\circ}35'10.31'' \pm 4.90''$	4.94 ± 0.49	3.05 ± 0.23	3.75 ± 0.14
NGC 1652	$04^{\text{h}}38^{\text{m}}22.86^{\text{s}} \pm 0.33^{\text{s}}$	$-68^{\circ}40'20.78'' \pm 4.96''$	2.70 ± 0.28	2.56 ± 0.17	2.29 ± 0.09
NGC 1718	$04^{\text{h}}52^{\text{m}}25.66^{\text{s}} \pm 0.19^{\text{s}}$	$-67^{\circ}03'06.91'' \pm 2.79''$	3.45 ± 0.32	3.06 ± 0.19	2.61 ± 0.09
NGC 1783	$04^{\text{h}}59^{\text{m}}09.29^{\text{s}} \pm 0.40^{\text{s}}$	$-65^{\circ}59'15.67'' \pm 6.02''$	5.63 ± 0.59	2.84 ± 0.20	4.46 ± 0.11
NGC 1806	$05^{\text{h}}02^{\text{m}}11.35^{\text{s}} \pm 0.22^{\text{s}}$	$-67^{\circ}59'09.56'' \pm 3.26''$	4.31 ± 0.56	2.77 ± 0.27	3.47 ± 0.17
NGC 1831	$05^{\text{h}}06^{\text{m}}16.55^{\text{s}} \pm 0.18^{\text{s}}$	$-64^{\circ}55'07.62'' \pm 2.73''$	6.66 ± 0.78	4.08 ± 0.47	4.23 ± 0.19
NGC 1841	$04^{\text{h}}45^{\text{m}}22.84^{\text{s}} \pm 1.00^{\text{s}}$	$-83^{\circ}59'47.32'' \pm 14.98''$	12.69 ± 1.82	5.12 ± 0.76	7.07 ± 0.39
NGC 1846	$05^{\text{h}}07^{\text{m}}33.86^{\text{s}} \pm 0.36^{\text{s}}$	$-67^{\circ}27'37.95'' \pm 5.40''$	5.58 ± 0.57	2.35 ± 0.21	5.01 ± 0.20
NGC 1852	$05^{\text{h}}09^{\text{m}}24.12^{\text{s}} \pm 0.34^{\text{s}}$	$-67^{\circ}46'46.92'' \pm 5.15''$	6.42 ± 0.92	3.44 ± 0.54	4.52 ± 0.26
NGC 1868	$05^{\text{h}}14^{\text{m}}35.74^{\text{s}} \pm 0.12^{\text{s}}$	$-63^{\circ}57'14.51'' \pm 1.78''$	2.06 ± 0.26	3.15 ± 0.23	1.53 ± 0.07
NGC 1978	$05^{\text{h}}28^{\text{m}}45.21^{\text{s}} \pm 0.31^{\text{s}}$	$-66^{\circ}14'13.55'' \pm 4.65''$	5.06 ± 0.73	3.37 ± 0.33	3.61 ± 0.19
NGC 2154	$05^{\text{h}}57^{\text{m}}38.24^{\text{s}} \pm 0.21^{\text{s}}$	$-67^{\circ}15'43.01'' \pm 3.16''$	4.37 ± 0.35	3.05 ± 0.20	3.31 ± 0.12
NGC 2173	$05^{\text{h}}57^{\text{m}}58.35^{\text{s}} \pm 0.27^{\text{s}}$	$-72^{\circ}58'43.85'' \pm 4.01''$	4.06 ± 0.58	2.96 ± 0.39	3.14 ± 0.17
NGC 2203	$06^{\text{h}}04^{\text{m}}43.07^{\text{s}} \pm 0.50^{\text{s}}$	$-75^{\circ}26'15.98'' \pm 7.49''$	4.83 ± 0.46	2.65 ± 0.17	4.00 ± 0.14
NGC 2209	$06^{\text{h}}08^{\text{m}}36.26^{\text{s}} \pm 0.76^{\text{s}}$	$-73^{\circ}50'22.44'' \pm 10.28''$	9.91 ± 1.99	3.94 ± 1.05	6.43 ± 0.55
NGC 2213	$06^{\text{h}}10^{\text{m}}41.95^{\text{s}} \pm 0.22^{\text{s}}$	$-71^{\circ}31'46.59'' \pm 3.32''$	3.00 ± 0.38	3.31 ± 0.34	2.16 ± 0.10
NGC 2249	$06^{\text{h}}25^{\text{m}}49.71^{\text{s}} \pm 0.20^{\text{s}}$	$-68^{\circ}55'14.66'' \pm 3.00''$	2.92 ± 0.24	3.00 ± 0.18	2.24 ± 0.07
NGC 2257	$06^{\text{h}}30^{\text{m}}12.39^{\text{s}} \pm 0.46^{\text{s}}$	$-64^{\circ}19'34.71'' \pm 6.94''$	14.27 ± 1.31	4.60 ± 0.87	8.46 ± 0.53
NGC 419	$01^{\text{h}}08^{\text{m}}17.12^{\text{s}} \pm 0.34^{\text{s}}$	$-72^{\circ}53'03.66'' \pm 5.04''$	7.02 ± 0.83	4.39 ± 0.44	4.28 ± 0.19

^aThe uncertainty was estimated by means of a bootstrap test.

NOTE—(1) Cluster name; (2,3) Central coordinates; (4) EFF core radius; (5) EFF concentration parameter; (6) King core radius.

follow $N_{\text{BS},c} \approx \tau_{\text{BS}}/\tau_{\text{coll}}$, where τ_{BS} is the typical BSS lifetime and τ_{coll} is the single star–single star collision timescale in the cluster core. If, on the other hand, binary stars are the primary BSS progenitors, their numbers are expected to be proportional to both the core mass, M_{core} , and the binary fraction, f_{bin} .

All previous work in this field (Knigge et al. 2009; Leigh et al. 2011a, 2013) has thus far concluded that scaling relations involving the core mass appear to yield the best estimate of the BSS numbers in a cluster’s core. To obtain accurate estimates of the total stellar mass contained within the core, we calculated membership probabilities using the structural parameters we derived based on our EFF profile fits:

$$P(r) = \frac{\rho(r) - \rho_{\text{bkg}}}{\rho_{\text{bkg}}}. \quad (3)$$

Next, we generated a synthetic cluster using the Monto Carlo method, adopting a Kroupa stellar initial mass function (IMF; Kroupa 2001),

$$\xi(m) \propto m^{-\alpha_i} \quad (4)$$

where

$$\begin{aligned} \alpha_0 &= 0.3, & 0.01 \leq m/M_\odot < 0.08; \\ \alpha_1 &= 1.3, & 0.08 \leq m/M_\odot < 0.50; \\ \alpha_2 &= 2.3, & 0.50 \leq m/M_\odot. \end{aligned} \quad (5)$$

The best-fitting isochrone provided the upper and lower boundaries to the initial mass of the remaining stars in the cluster, which served as the integral range adopted for the IMF (Column 6 in Table 3). The initial mass, generated through Monto Carlo sampling of the IMF, was interpolated back to the isochrone to generate a mock cluster with

Table 3. Best-fitting isochrones and masses for our MC sample clusters.

Cluster	$\log(t \text{ yr}^{-1})$	Z^a	A_V (mag)	$(m - M)_0$ (mag)	$m_{\text{ini}} (M_\odot)$	$\log \rho_0 (M_\odot \text{ pc}^{-3})$	$\log M (M_\odot)$
(1)	(2)	(3)	(4)	(5)	(6)	(7)	(8)
ESO057–SC075	9.25 ± 0.05	0.006 ± 0.001	0.18 ± 0.02	18.42 ± 0.03	1.66	1.20 ± 0.20	3.87 ± 0.13
Hodge 11	10.09 ± 0.05	0.00025 ± 0.001	0.24 ± 0.02	18.50 ± 0.03	0.80	2.20 ± 0.03	5.27 ± 0.03
IC 2146	9.30 ± 0.05	0.007 ± 0.001	0.08 ± 0.02	18.55 ± 0.03	1.57	0.71 ± 0.15	4.31 ± 0.09
NGC 1466	10.10 ± 0.05	0.0003 ± 0.001	0.22 ± 0.02	18.43 ± 0.03	0.80	2.51 ± 0.08	5.20 ± 0.03
NGC 1644	9.23 ± 0.05	0.006 ± 0.001	0.03 ± 0.02	18.48 ± 0.03	1.69	1.92 ± 0.19	3.91 ± 0.14
NGC 1651	9.30 ± 0.05	0.006 ± 0.001	0.31 ± 0.02	18.48 ± 0.03	1.59	1.50 ± 0.12	4.32 ± 0.09
NGC 1652	9.33 ± 0.05	0.005 ± 0.001	0.186 ± 0.02	18.48 ± 0.03	1.53	1.65 ± 0.19	3.91 ± 0.12
NGC 1718	9.24 ± 0.05	0.007 ± 0.001	0.53 ± 0.02	18.63 ± 0.03	1.70	2.15 ± 0.09	4.52 ± 0.07
NGC 1783	9.25 ± 0.05	0.005 ± 0.001	0.06 ± 0.02	18.46 ± 0.03	1.64	2.05 ± 0.05	5.00 ± 0.04
NGC 1806	9.26 ± 0.05	0.005 ± 0.001	0.10 ± 0.02	18.48 ± 0.03	1.62	2.10 ± 0.06	4.71 ± 0.05
NGC 1831	8.85 ± 0.05	0.008 ± 0.001	0.12 ± 0.02	18.40 ± 0.03	2.46	1.65 ± 0.12	4.53 ± 0.09
NGC 1841	10.05 ± 0.05	0.00025 ± 0.001	0.56 ± 0.02	18.38 ± 0.03	0.83	1.44 ± 0.02	5.22 ± 0.03
NGC 1846	9.28 ± 0.05	0.006 ± 0.001	0.07 ± 0.02	18.45 ± 0.03	1.62	1.60 ± 0.06	4.76 ± 0.05
NGC 1852	9.20 ± 0.05	0.006 ± 0.001	0.15 ± 0.02	18.46 ± 0.03	1.74	1.32 ± 0.11	4.25 ± 0.08
NGC 1868	9.10 ± 0.05	0.006 ± 0.001	0.12 ± 0.02	18.40 ± 0.03	1.96	2.75 ± 0.11	4.39 ± 0.10
NGC 1978	9.40 ± 0.05	0.005 ± 0.001	0.10 ± 0.02	18.55 ± 0.03	1.45	2.54 ± 0.03	5.19 ± 0.03
NGC 2154	9.27 ± 0.05	0.005 ± 0.001	0.064 ± 0.02	18.48 ± 0.03	1.61	1.67 ± 0.02	4.32 ± 0.08
NGC 2173	9.23 ± 0.05	0.007 ± 0.001	0.24 ± 0.02	18.45 ± 0.03	1.71	1.93 ± 0.13	4.82 ± 0.10
NGC 2203	9.24 ± 0.05	0.008 ± 0.001	0.19 ± 0.02	18.40 ± 0.03	1.72	1.54 ± 0.12	4.49 ± 0.07
NGC 2209	9.16 ± 0.05	0.008 ± 0.001	0.20 ± 0.02	18.45 ± 0.03	1.92	0.65 ± 0.16	4.07 ± 0.11
NGC 2213	9.24 ± 0.05	0.008 ± 0.001	0.16 ± 0.02	18.40 ± 0.03	1.72	2.01 ± 0.16	4.10 ± 0.13
NGC 2249	9.00 ± 0.05	0.006 ± 0.001	0.12 ± 0.02	18.40 ± 0.03	2.13	2.00 ± 0.16	4.09 ± 0.12
NGC 2257	10.02 ± 0.05	0.0005 ± 0.001	0.20 ± 0.02	18.48 ± 0.03	0.84	1.80 ± 0.03	5.05 ± 0.03
NGC 419	9.20 ± 0.05	0.0025 ± 0.001	0.181 ± 0.02	18.90 ± 0.03	1.57	2.33 ± 0.09	5.05 ± 0.04

^a $Z_\odot = 0.0152$

NOTE—(1) Cluster name; (2) Best-fitting cluster age (logarithmic units); (3) Metallicity; (4) Extinction; (5) Distance modulus; (6) Upper boundary to the initial stellar mass used to estimate the cluster mass; the lower boundary we adopted is $0.09 M_\odot$; (7) Central volume density; (8) Cluster mass.

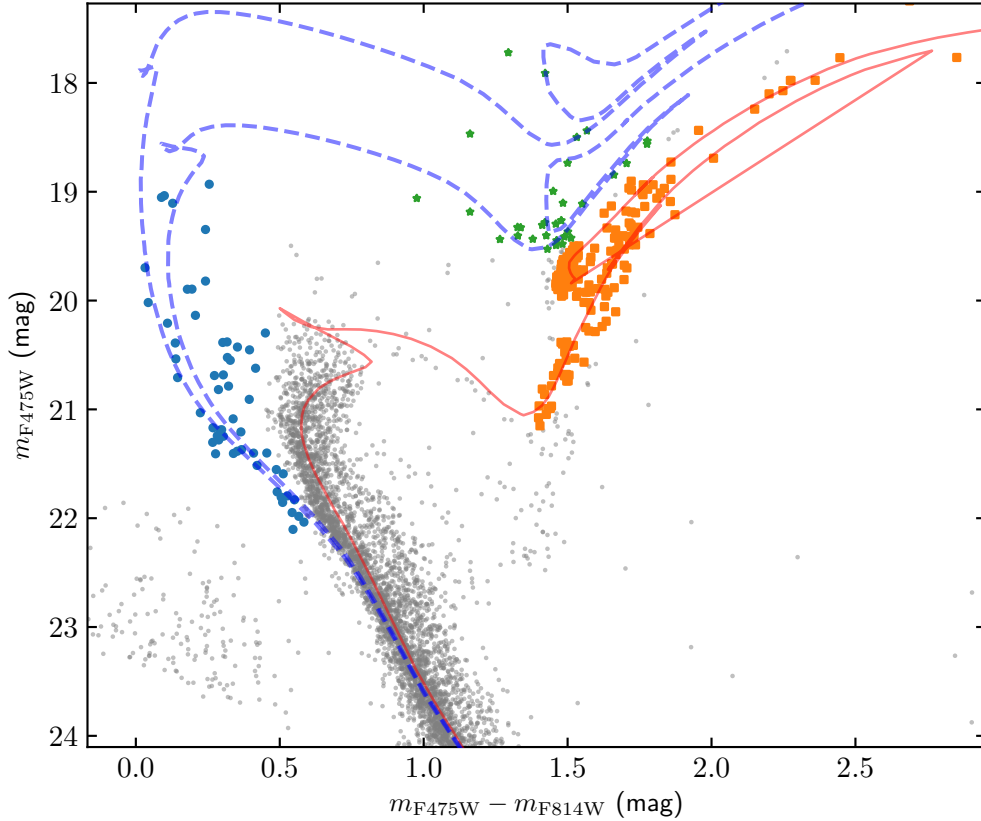


Figure 1. NGC 2173 CMD. BSSs, evolved BSSs, and RGB stars are marked with blue circles, green pentagons, and orange squares, respectively. The best-fitting isochrones for the bulk stellar population (red solid line) and the young population (blue dashed line) are also shown. The CMDs pertaining to all other clusters are available in the Figure Set.

the same age as the real cluster of interest. The population of MS stars within 2 magnitudes below the MSTO was used as control group (Xin et al. 2007), given that they are not significantly affected by sampling incompleteness. The stellar numbers in the control group (corrected for their membership probabilities) in the real and synthetic clusters are proportional to their masses. We then multiplied the integrated mass thus obtained for the synthetic cluster by this ratio to estimate the total stellar mass contained within one core radius from the real cluster’s center as well as the cluster’s integrated mass (see column 8 in Table 3).

We found a proportionality of the type $N_{\text{BSS},c} \propto M_c^{0.66 \pm 0.07}$ (see Fig. 2, left). The uncertainty in the power-law index was estimated based on a series of bootstrapping experiments. We created 1000 realizations and fitted a linear relation to estimate the resulting confidence intervals. A Spearman test indicates that the BSS numbers and cluster core masses are strongly correlated, $\rho_S = 0.84$. Since the Spearman coefficient is significantly different from either unity (by 4.8σ) or zero (by 9.4σ), we confirm this sublinear relation robustly. Although the resulting power-law index is slightly larger than the value of ~ 0.5 found by Knigge et al. (2009) and Leigh et al. (2013), the discrepancies are within 2σ .

Upon inclusion of the evolved BSSs (Fig. 2, right), the proportionality becomes $N_{\text{BSS},c} \propto M_c^{0.51 \pm 0.07}$, with a Spearman coefficient of $\rho_S = 0.80$. Now the difference in power-law indices between our result and those published previously is less than 1σ , suggesting that the BSSs in MC clusters are characterized by a very similar correlation as their counterparts in the Milky Way. Fig. 2 shows that the evolved BSSs are distinguished unequivocally only in our intermediate-age clusters. In old clusters, the locus of the evolved population is closely coincident with that of the red clump (RC) stars. This is so, because in optical filters the locus of the RC stars does not change significantly for

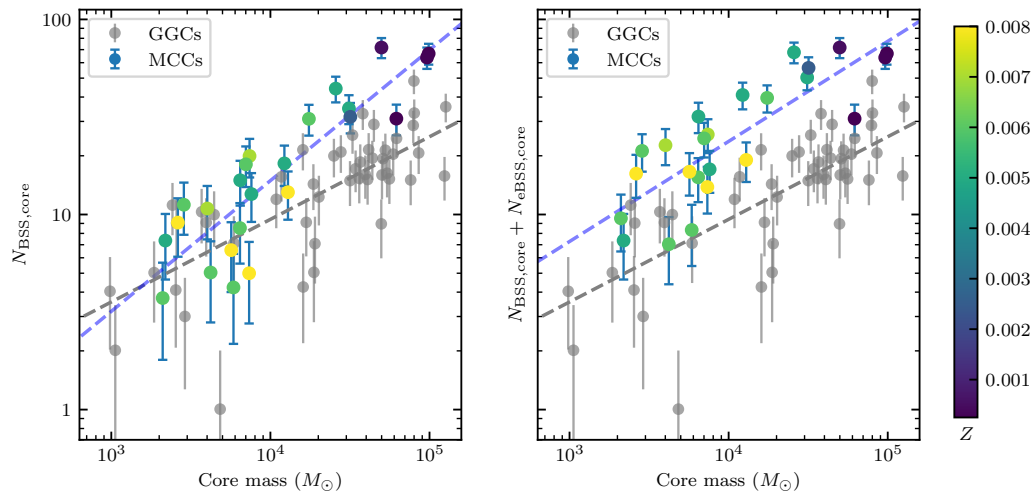


Figure 2. Number of core BSSs ($N_{\text{BSS,core}}$; left) and BSS populations including evolved BSSs ($N_{\text{eBSS,core}}$; right) versus the core masses of our clusters. Colorful dots correspond to MC clusters (MCCs; colors represent the clusters’ metallicities, Z), grey dots to Galactic GCs (GGCs, Knigge et al. 2009). The error bars shown are the approximate 68% Poissonian confidence intervals. The blue and grey dashed lines represent the best power-law fits to the data.

ages in excess of 2 Gyr, thus rendering evolved BSSs indistinguishable from RC stars associated with a cluster’s bulk stellar population isochrone. Parada et al. (2016) reported the existence of such a population in 47 Tuc using *HST* data obtained in UV filters.

As we have seen, the power-law index becomes smaller when the evolved BSSs are included in the analysis. Although the Spearman test yields a less significant correlation for samples including evolved BSSs compared with ‘clean’ samples without such evolved objects, the statistical robustness is more significant for correlations involving cluster core masses than for any other cluster parameters (Leigh et al. 2013).

Second, Knigge et al. (2009) predicted that the number of BSSs and the number of binary stars in the core should be correlated, which was confirmed by Leigh et al. (2013). However, the large distance to the MCs renders most methods commonly used to explore this effect in Galactic GCs useless. Milone et al. (2012) measured MS binary fractions by comparing (in a minimum- χ^2 sense) simulated CMDs characterized by a series of different binary fractions with their observational data. Similarly, Hu et al. (2010) compared synthetic CMDs characterized by different binary fractions with observational data for the young MC cluster NGC 1818. Since we are only able to detect high-mass-ratio binaries in the CMDs of our MC clusters, the global binary fractions for all mass ratios rely on the validity of the assumed mass-ratio distribution. Note, however, that binary determinations based on CMD analysis can only be done robustly for MS binaries, and not for binaries at the MSTO, where most observable BSSs are expected to originate. This is a serious problem affecting all studies attempting to deal with BSS formation based on CMD analysis (Goudfrooij et al. 2014), which is further compounded by the hotly debated physics at play in extended MSTO regions.

In Fig. 3, we show the number of core BSSs as a function of the collision rate, both normalized to the cluster mass. The mass-normalized quantities are defined, respectively, as $n_{\text{BSS}} \equiv N_{\text{BSS}}/(M/10^5 M_{\odot})$ and $\gamma \equiv \Gamma/(M/10^5 M_{\odot})$, where the collision parameter Γ , approximately the annual stellar collision rate, is given by

$$\Gamma = \left(\frac{\rho_0}{M_{\odot} \text{pc}^{-3}} \right)^2 \left(\frac{r_c}{\text{pc}} \right)^3 \left(\frac{v_{c,\sigma}}{\text{km s}^{-1}} \right)^{-1}, \quad (6)$$

where ρ_0 is the central mass volume density, r_c is the core radius, and σ is the central velocity dispersion (Pooley & Hut 2006). We introduced mass-normalized parameters to alleviate the problem associated with the presence of a Γ -mass correlation, that is, more massive clusters experience higher integrated collision numbers, and vice versa. Following Pooley & Hut (2006), we assumed both primordial and dynamical contributions: $n = C + a\gamma^b$. Here, C represents the fraction of the contribution that is independent of the collision properties and which has a primordial origin (e.g., primordial binary systems), while the second term on the right-hand side of the equation represents the

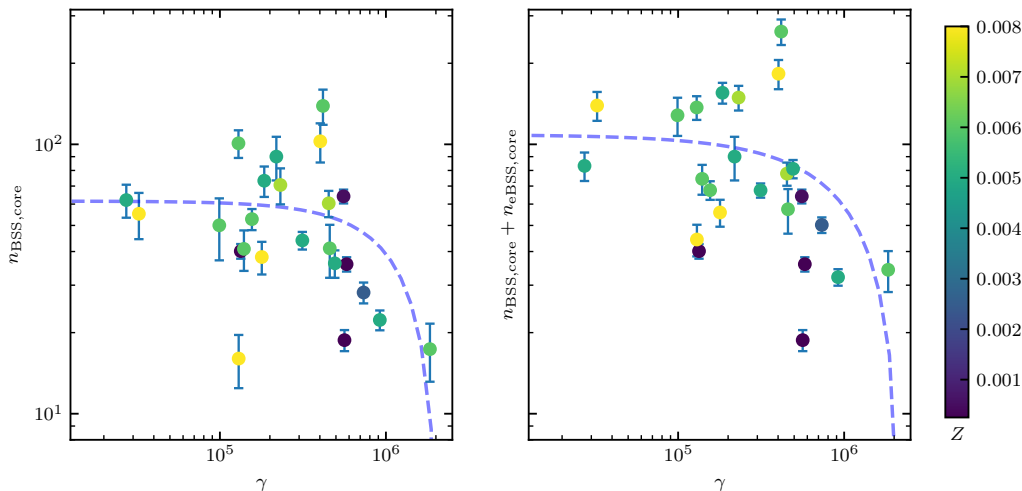


Figure 3. As Fig. 2, but for the mass-normalized number of BSSs in the core ($n_{\text{BSS,core}}$) versus the mass-normalized collision parameter, γ . The blue dashed line represents the best-fitting model of the form $n = C + a\gamma^b$.

fraction of the contribution that is related to dynamical interactions in the cluster. Fig. 3 shows a decreasing trend for larger γ , although the spread is significant. The normalized number of BSSs may exhibit a weak (or perhaps no) dependence on the collision rate for $\gamma \leq 3 \times 10^5$, suggesting that a collision-dominated BSS formation mechanism is ruled out. For larger γ , collisions do not enhance but instead suppress the formation of BSSs. This could be caused by the effects of disruption due to close encounters on the numbers of primordial binaries. Since BSSs formed from binaries represent the majority of a BSS population, this difference in primordial binary fraction could also explain the large spread. In the next section, we will discuss the interpretation of this result in detail.

To provide a direct probe of the BSS populations in various clusters, we introduce the specific frequency of BSSs, defined as the ratio of the number of BSSs to that of a reference population. Numerous approaches have been used to estimate this parameter (Ferraro et al. 1995). Here, we adopt $N_{2,\text{core}}$ as the reference population. N_2 is defined as the number of stars within a 2 mag interval below the MSTO. We also estimated the specific frequency by normalizing to the number of RGB stars (Fig. 1). Our results were identical no matter which reference population we used. Therefore, we adopted $N_{2,\text{core}}$ as our reference population, yielding in turn F_{BSS} . Moreover, we inspected the correlation, if any, of F_{BSS} with $N_{2,\text{core}}$ rather than with core mass or core stellar number, because the number of BSSs is more reliable and robust than the core mass and, by virtue of their brightness, less affected by the level of incompleteness.

We obtained reliable anti-correlations with N_2 , resulting in power-law indices of -0.43 ± 0.06 and -0.56 ± 0.07 for BSSs and BSSs combined with evolved BSSs, respectively. Both values differ by 6σ from zero; Spearman tests resulted in coefficients $\rho_S = -0.66$ and -0.73 , respectively. Generally, $N_{2,\text{core}}$ should be proportional to a cluster’s luminosity, M_V , so this is also a strong indication of the presence of an anti-correlation with total brightness. Therefore, this type of relation, which was first reported by Piotto et al. (2004) for Galactic GCs, has thus been confirmed to apply to MC clusters as well.

4. DISCUSSION

We found a strong correlation between the number of BSSs in the core and core mass, $N_{\text{BSS,c}} \propto M_c^{0.51 \pm 0.07}$, in our MC clusters, whereas we did not find any strong dependence on the collision rate in low-collision-rate clusters. In fact, higher collision rates suppress the formation efficiency of BSSs. Therefore, we suspect that this may be evidence of the predominance of the BSS binary formation channel. To quantify the possible contributions from the binary and the collision channels, we reproduced Fig. 3 based on the simulations of Chatterjee et al. (2013). Numerical simulations have been widely applied to study the formation of BSSs in dense globular clusters. They provide a unique method to explore the formation channel of individual BSSs. Hypki & Giersz (2013, 2017) conducted Monte Carlo simulations of dense GCs and investigated the dependence of the dominant type of BSSs on the initial cluster conditions. Chatterjee et al. (2013) found that the collision channel increases in importance with increasing central density. They reproduced

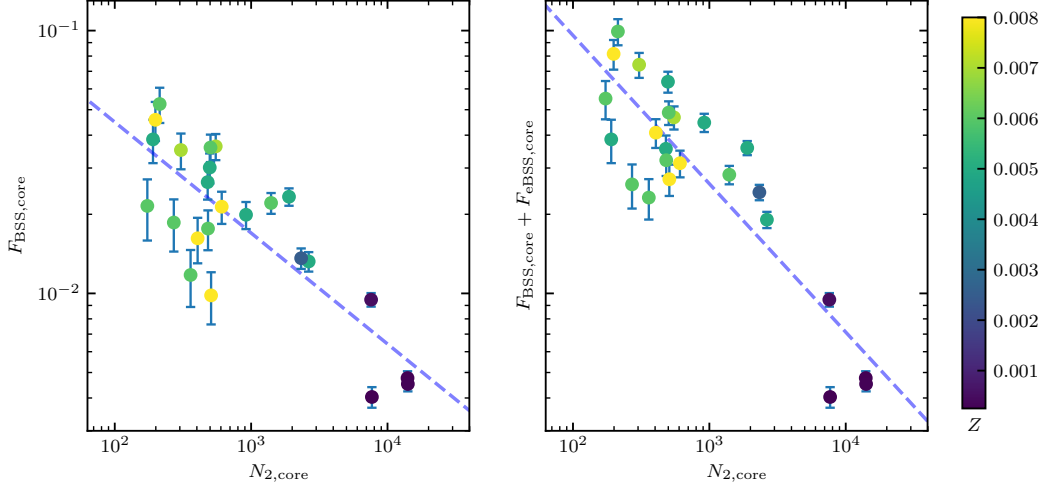


Figure 4. As Fig. 2, but for the specific frequency of BSSs ($F_{\text{BSS,core}}$) versus $N_{2,\text{core}}$. The specific frequencies of BSS and evolved BSS in the core are indicated by the subscripts ‘BSS’ and ‘eBSS,’ respectively.

the well-established correlation between the number of BSSs in the cluster core with Γ . Subsequently, [Sills, et al. \(2013\)](#) carried out mock observations of their simulated clusters and investigated correlations between their BSSs and various cluster properties. They concluded that the strong correlation of $N_{\text{BSS,c}}$ with cluster core mass and the weak dependence on Γ found in recent observations can be reconstructed in their models if most BSSs are created through binary-mediated collisions. These result therefore do not support the idea that the binary formation channel could dominate in GCs.

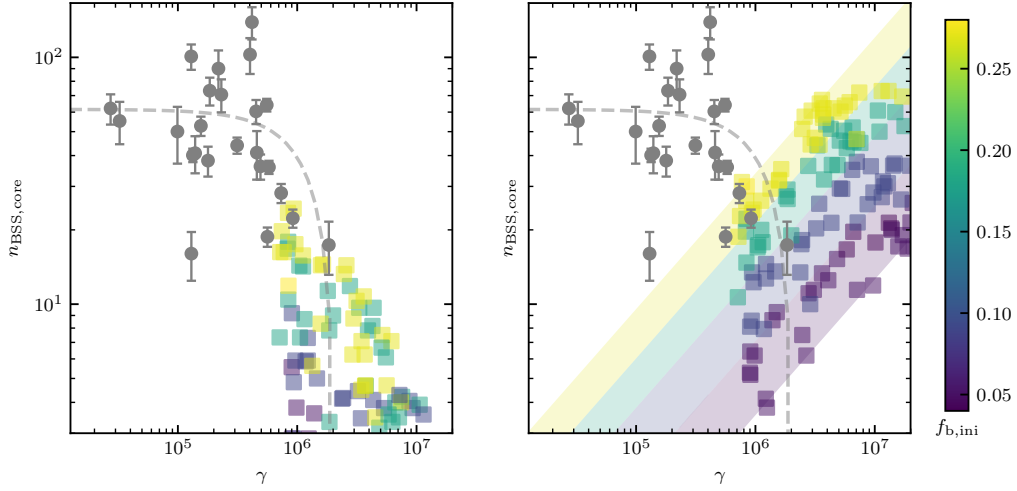


Figure 5. As Fig. 3, but with the simulation of [Chatterjee et al. \(2013\)](#) overplotted. The MCCs’ mass-normalized numbers of BSSs in the core ($n_{\text{BSS,core}}$) versus the mass-normalized collision parameter γ are shown as grey dots, and the best-fitting models are shown as grey dashed lines (as in the left-hand panel of Fig. 3). BSSs formed through the binary and collision channels in the simulation are presented, respectively, in the left- and right-hand panels as colorful squares, with different initial binary fractions ($f_{\text{b,ini}}$) indicated by different colors. The shaded regions encompass the possible contributions from collisions in lower collision-rate environments.

Fig. 5 includes the simulation result of [Chatterjee et al. \(2013, their Table 1\)](#). BSSs formed through the binary and collision channels are shown as colorful squares, respectively, in the left- and right-hand panels, with different initial

binary fractions indicated by different colors. We extrapolated the contribution from collisions toward lower collision rates (shadowed regions). We caution, however, that the collisional Γ given by Eq. 6 only predicts BSS formation through single–single star collisions (Chatterjee et al. 2013). A series of simulations has proved that the probability of collisions involving more than two stars is more significant by orders of magnitude in a binary-mediated model (e.g. Fregeau, et al. 2004; Chatterjee et al. 2013; Sills, et al. 2013), since single–binary, binary–binary, and higher-order collisions have much larger collisional cross sections than single–single star collisions. Based on Fig. 5 we suggest that the collision parameter shows a correlation for higher-order collisions; the actual share appears to be regulated by the fractions of binary or triple systems.

Chatterjee et al. (2013) explored a simulation grid covering star clusters with observed central densities $\rho_{c,\text{obs}}$ between $\approx 3 \times 10^2$ and $4 \times 10^6 M_\odot \text{pc}^{-3}$, whereas the densities of our MCCs (see Table 3) are generally lower than those of Galactic GCs by an order of magnitude. Although the simulations only marginally overlap with our observational parameter space, they are indeed adequate to offer insights into the driving mechanism of BSS formation in our sample clusters. The left-hand panel of Fig. 5 shows that the mass-normalized number of BSSs generated from primordial binaries in the simulation declines toward higher collision rates, as observed in the MCCs, while the collision model predicts an opposite tendency. This suggests that binary disruption may be at work. Extrapolating, we estimate that the share contributed by the collision channel in lower collision-rate environments is less than 20%, demonstrating a more significant contribution from the binary channel. Those clusters characterized by $7 \times 10^5 \leq \gamma \leq 2 \times 10^6$ may be interpreted as spanning a transition phase between primordial-binary-dominated and collision-dominated systems, where γ is, on the one hand, large enough to suppress BSS production via the binary channel, but on the other hand not high enough to form collisional BSSs efficiently.

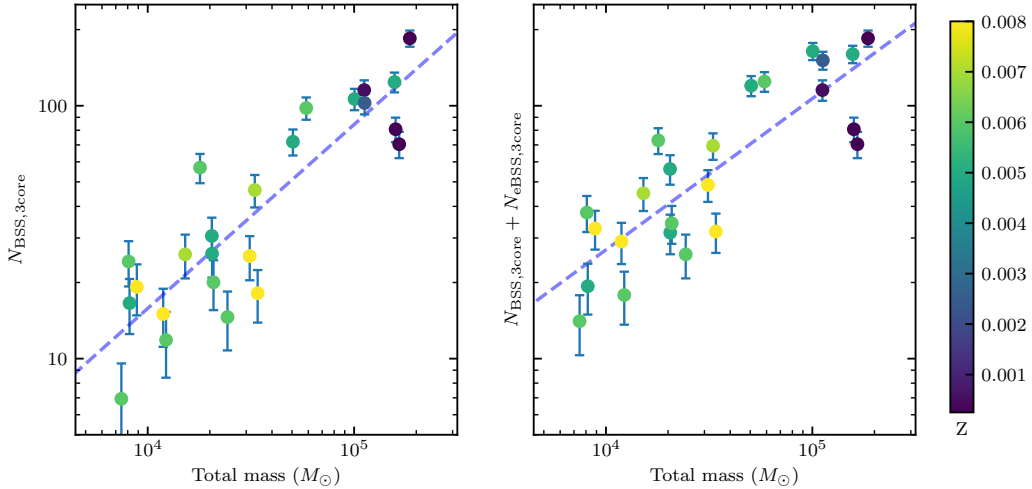


Figure 6. As Fig. 2, but for the number of BSSs within $3 r_c$ versus total mass.

We also checked the number of BSSs within a larger radial range ($3 r_c$; see Fig. 6) and found that the correlation with core (or total) mass was almost identical to the earlier results (yielding power-law indices of 0.72 ± 0.08 and 0.60 ± 0.08). This implies that the dominant BSS formation channel appears universal across the cluster, which would not be expected if the collision scenario were dominant. If the formation of BSSs in these clusters is mainly attributed to mass transfer in binary systems, we can assume the number of BSSs to scale with the number of binary stars, $N_{\text{BSS}} \propto N_{\text{bin}} \propto f_{\text{bin}} M$. The proportionality $N_{\text{BSS},c} \propto M_c^{0.51 \pm 0.07}$ suggests that the binary fraction is anti-correlated with core mass, with a power-law index of -0.5 . This is also confirmed by Fig. 4, where the BSS specific frequency should scale with binary fraction in the binary-formation scenario. Such an anti-correlation between binary fraction and core mass has already been found for Galactic GCs (Milone et al. 2012), but this is the first time that such a relation is demonstrated for MC clusters. As a cluster evolves for several relaxation times, dynamical mass segregation causes binaries to sink toward the center of the cluster’s gravitational potential well, thus increasing the binary fraction, although strong dynamical interactions can, in turn, destroy binaries. This process is at the basis of the regulation of

the binary fraction in GCs (Fregeau et al. 2009). Most of our sample clusters are young or of intermediate dynamical age (their ages are comparable to their half-mass relaxation timescales), so the effects of mass segregation should be relatively minor. The dynamical interaction rates are also limited because of the relatively low stellar densities. Therefore, it is interesting that we have found that the same general anti-correlation exists in a completely distinct environment.

5. CONCLUSIONS

We analyzed the CMDs of 24 star clusters in the Magellanic Clouds using multi-passband *HST* images. We constructed a homogeneous database of BSSs and their evolutionary products. We studied the properties of the BSSs relative to the clusters' core masses, and compared our BSS observations with the numbers expected from collision and binary formation models. Our main results and conclusions are summarized below:

- BSSs are found in all of our clusters, with BSS numbers in their cores ranging from five to 70. Evolved BSSs can be resolved in the intermediate-age clusters using optical bands, whereas they cannot be disentangled easily from the RC in old clusters. After field decontamination, we verified that these BSS populations likely represent genuine cluster members.
- We confirmed that the correlation between the number of BSSs in a cluster's core with its core mass is valid in MC clusters, with power-law indices of 0.66 ± 0.07 (only BSSs) or 0.51 ± 0.07 (including evolved BSSs). The discrepancy with previously published results is of order 1 to 2σ . The mass-normalized number of BSSs shows little dependence on the mass-normalized collision parameter for $\gamma \leq 3 \times 10^5$; a decreasing trend with increasing collision parameter was found for larger collision rates, which is likely due to binary disruption. A comparison with Chatterjee et al. (2013)'s simulations disfavors the collision channel and supports a dominant binary channel, defined by a contribution in excess of 80% in lower collision-rate clusters ($\gamma \leq 3 \times 10^5$).
- Since for the numbers of BSSs within a large radial range we still find a similar correlation with cluster mass, mass-transfer binaries are most likely the progenitors of the BSSs in most of our MC sample clusters. The anti-correlation of the BSS specific frequency with core mass further underscores this argument. This also implies an anti-correlation between the binary fraction and core mass.
- We argue that MCCs represent a special environment for the study of BSS formation in clusters. Although the correlation of the number of BSSs with core mass in the MCCs is quite similar to that in Galactic GCs, the underlying formation channels might be different. The low stellar density (or collision rate) of MCCs provides a great opportunity to resolve the tension between observations and simulations in the interpretation of the correlation in Galactic GCs, which deserves further study.

We thank J. Hong for enlightening discussions about simulation aspects. C.L. acknowledges funding support from the Macquarie Research Fellowship Scheme. R.d.G. and L.D. acknowledge research support from the National Natural Science Foundation of China through grants 11633005, 11473037, and U1631102. R.d.G. is grateful for support from the National Key Research and Development Program of China through grant 2017YFA0402702 from the Chinese Ministry of Science and Technology (MOST). L.D. also acknowledges support from MOST through grant 2013CB834900.

Software: dolphot2.0 (Dolphin 2000), PARSEC (1.2S; Bressan et al. 2012), Astropy (Astropy Collaboration et al. 2013), Matplotlib (Hunter 2007)

REFERENCES

- | | |
|---|--|
| <p>Astropy Collaboration, Robitaille, T. P., Tollerud, E. J., et al. 2013, <i>A&A</i>, 558, A33</p> <p>Bica, E., Bonatto, C., Dutra, C. M., & Santos, J. F. C. 2008, <i>MNRAS</i>, 389, 678</p> | <p>Bressan, A., Marigo, P., Girardi, L., et al. 2012, <i>MNRAS</i>, 427, 12</p> <p>Chatterjee, S., Rasio, F. A., Sills, A., & Glebbeek, E. 2013, <i>ApJ</i>, 777, 106</p> <p>Chen, X., & Han, Z. 2008, <i>MNRAS</i>, 384, 1263</p> |
|---|--|

- Dolphin, A. E. 2000, *PASP*, 112, 1383
- Elson, R. A. W. 1991, *ApJS*, 76, 185
- Elson, R. A. W., Fall, S. M., & Freeman, K. C. 1989, *ApJ*, 336, 73
- Ferraro, F. R., Beccari, G., Dalessandro, E., et al. 2009, *Nature*, 462, 1028
- Ferraro, F. R., Fusi Pecci, F., & Bellazzini, M. 1995, *A&A*, 294, 80
- Ferraro, F. R., Paltrinieri, B., Fusi Pecci, F., et al. 1997, *ApJL*, 484, L145
- Ferraro, F. R., Paltrinieri, B., Rood, R. T., & Dorman, B. 1999, *ApJ*, 522, 983
- Ferraro, F. R., Sills, A., Rood, R. T., Paltrinieri, B., & Buonanno, R. 2003, *ApJ*, 588, 464
- Fregeau, J. M., Ivanova, N., & Rasio, F. A. 2009, *ApJ*, 707, 1533
- Fregeau, J. M., Cheung, P., Portegies Zwart, S. F., et al. 2004, *MNRAS*, 352, 1
- Goudfrooij, P., Girardi, L., Kozhurina-Platais, V., et al. 2014, *ApJ*, 797, 35
- Hu, Y., Deng, L., de Grijs, R., Liu, Q., & Goodwin, S. P. 2010, *ApJ*, 724, 649
- Hunter, J. D. 2007, *Computing in Science and Engineering*, 9, 90
- Hypki, A. & Giersz, M. 2013, *MNRAS*, 429, 1221
- Hypki, A. & Giersz, M. 2017, *MNRAS*, 466, 320
- Iben, I., Jr., & Tutukov, A. V. 1984, *ApJ*, 284, 719
- King, I. 1962, *AJ*, 67, 471
- Knigge, C., Leigh, N., & Sills, A. 2009, *Nature*, 457, 288
- Kroupa, P. 2001, *MNRAS*, 322, 231
- Leigh, N., Knigge, C., Sills, A., et al. 2013, *MNRAS*, 428, 897
- Leigh, N., Sills, A., & Knigge, C. 2011, *MNRAS*, 415, 3771
- Leigh, N., Sills, A., & Knigge, C. 2011, *MNRAS*, 416, 1410
- Leigh, N., Sills, A. & Knigge, C. 2007, *ApJ*, 661, 210
- Li, C., de Grijs, R., & Deng, L. 2013, *MNRAS*, 436, 1497
- Li, C., de Grijs, R., Deng, L., et al. 2016, *Nature*, 529, 502
- Li, C. & Hong, J. 2018, *MNRAS*, 476, 5274.
- Mackey, A. D., & Gilmore, G. F. 2003, *MNRAS*, 338, 85
- Mackey, A. D., & Gilmore, G. F. 2003, *MNRAS*, 338, 120
- Mapelli, M., Ripamonti, E., Tolstoy, E., et al. 2007, *MNRAS*, 380, 112
- Mapelli, M., Sigurdsson, S., Ferraro, F. R., et al. 2006, *MNRAS*, 373, 361
- Martocchia, S., Bastian, N., Usher, C., et al. 2017, *MNRAS*, 468, 3150
- McCrea, W. H. 1964, *MNRAS*, 128, 147
- McLaughlin, D. E., & van der Marel, R. P. 2005, *ApJS*, 161, 304
- Milone, A. P., Piotto, G., Bedin, L. R., et al. 2012, *A&A*, 540, A1
- Mucciarelli, A., Origlia, L., & Ferraro, F. R. 2007, *AJ*, 134, 1813
- Niederhofer, F., Bastian, N., Kozhurina-Platais, V., et al. 2016, *A&A*, 586, A148OB
- Niederhofer, F., Hilker, M., Bastian, N., & Silva-Villa, E. 2015, *A&A*, 575, A62
- Parada, J., Richer, H., Heyl, J., Kalirai, J., & Goldsbury, R. 2016, *ApJ*, 830, 139
- Piatti, A. E. & Mackey, A. D. 2018, *MNRAS*, 991.
- Piotto, G., DeAngeli, F., King, I. R., et al. 2004, *ApJL*, 604, L109
- Pooley, D. & Hut, P. 2006, *ApJ*, 646, L143
- Raso, S., Ferraro, F. R., Dalessandro, E., et al. 2017, *ApJ*, 839, 64
- Sandage, A. R. 1953, *AJ*, 58, 61
- Sills, A., Glebbeek, E., Chatterjee, S., et al. 2013, *ApJ*, 777, 105
- Sollima, A., Lanzoni, B., Beccari, G., et al. 2008, *A&A*, 481, 701
- Wagner-Kaiser, R., Mackey, D., Sarajedini, A., et al. 2017, *MNRAS*, 471, 3347
- Xin, Y., Deng, L., & Han, Z. W. 2007, *ApJ*, 660, 319